Research Article | Vol. 28, No. 23 / 9 November 2020 / Optics Express 33937
Optics EXPRESS

High-resolution microscopy through optically opaque media using ultrafast photoacoustics

ALESSANDRO ANTONCECCHI,[1,2,4] HAO ZHANG,[1,2] STEPHEN EDWARD,[1,3] VANESSA VERRINA,[1,3] PAUL C. M. PLANKEN,[1,3] AND STEFAN WITTE[1,2,5]

[1]*Advanced Research Center for Nanolithography, Science Park 106, 1098 XG Amsterdam, Netherlands*
[2]*Vrije Universiteit Amsterdam, De Boelelaan 1105, 1081 HV Amsterdam, Netherlands*
[3]*Universiteit van Amsterdam, Science Park 904, 1098 XH Amsterdam, Netherlands*
[4]*a.antoncecchi@arcnl.nl*
[5]*witte@arcnl.nl*

Abstract: We present a high-resolution microscope capable of imaging buried structures through optically opaque materials with micrometer transverse resolution and a nanometer-scale depth sensitivity. The ability to image through such materials is made possible by the use of laser ultrasonic techniques, where an ultrafast laser pulse launches acoustic waves inside an opaque layer and subsequent acoustic echoes from buried interfaces are detected optically by a time-delayed probe pulse. We show that the high frequency of the generated ultrasound waves enables imaging with a transverse resolution only limited by the optical detection system. We present the imaging system and signal analysis and demonstrate its imaging capability on complex microstructured objects through 200 nm thick metal layers and gratings through 500 nm thickness. Furthermore, we characterize the obtained imaging performance, achieving a diffraction-limited transverse resolution of 1.2 μm and a depth sensitivity better than 10 nm.

© 2020 Optical Society of America under the terms of the OSA Open Access Publishing Agreement

1. Introduction

Optical imaging methods are essential in many areas of science and technology. In the semiconductor industry, optical metrology tools are employed for rapid positioning and accurate quantitative inspection of layer-to-layer placement in lithographic devices [1,2]. This type of metrology requires high-numerical-aperture imaging systems to be sensitive to sub-micrometer-sized metrology markers. Semiconductor device architectures are becoming increasingly complex, leading to the use of sophisticated three-dimensional nanostructures for e.g. memory devices [3–5]. As such structures often contain materials that are optically opaque, imaging and metrology tools are needed that can detect metrology markers through layers of such opaque materials, while maintaining sufficient spatial resolution. Acoustic waves have the capability to propagate through almost any material. While acoustic metrology is often associated with larger scales, ultrafast-laser-induced acoustic waves [6–12] can actually reach frequencies up to the THz range [13–16], and therefore have remarkably short wavelengths. Photoacoustic methods can therefore provide contrast on micron-sized features commonly used in optical metrology, combined with the ability to detect such features through materials that are fully opaque to light. This combination of properties has already motivated the development of high-resolution photoacoustic imaging systems [17–19] using ultrafast-laser-induced ultrasound pulses. Daly et al. [17] demonstrated the possibility to detect and image sub-optical-wavelength features through acoustic diffraction.

In this paper, we present an optical microscope system that uses ultrafast laser driven ultrasound pulses for high-resolution imaging of complex microstructures through layers of opaque media. Both generation and probing of the ultrasound waves are performed from the same side, which is a fundamental requirement for substrate-based objects, enabling imaging of buried microscopic

#405875 https://doi.org/10.1364/OE.405875
Journal © 2020 Received 20 Aug 2020; revised 1 Oct 2020; accepted 15 Oct 2020; published 26 Oct 2020

Optics EXPRESS

features to which no optical access is possible, in a non-invasive way. Both temporal and spatial scans are performed to obtain a spatially resolved map of the local layer thickness, from which a 3D map of the buried structures is obtained. We performed such experiments on both periodic and non-periodic objects with feature sizes down to 500 nm. We also describe the analysis procedure and how that provides quantitative information, to determine the spatial resolution in transverse and axial dimensions (thickness). In addition, we demonstrate a faster imaging approach, in which a spatial scan is performed at fixed pump-probe time delay [18] to provide contrast in imaging buried objects.

2. Experimental methods

2.1. Pump-probe setup for time-dependent reflectivity measurements

Femtosecond lasers can generate high-frequency sound waves in metals through ultrafast and strongly localized absorption of radiation by the electron gas [6,9,10]. When a femtosecond pulse strikes a metal, the energy is initially mainly absorbed by the electrons, which subsequently equilibrate with the lattice on a timescale of picoseconds. This energy exchange leads to a rapid increase of the lattice temperature, generating a thermal stress that is the source for the acoustic waves. The resulting acoustic waves travel inside the metal and partially reflect off buried material interfaces. The returning reflected 'echo' is optically detectable at the surface, as the local lattice strain leads to changes in the complex refractive index. A measurement of the time-dependent metal reflectivity therefore reveals the presence of ultrasound-induced strain at the sample surface. To generate and detect laser-produced ultrasound pulses, a pump-probe scheme is implemented [13,14]. A schematic of the experimental setup is shown in Fig. 1. The output of a long-cavity Ti-sapphire oscillator (Femtolasers XL500: wavelength centered at 800 nm, pulse duration 70 fs, repetition rate 5.1 MHz) is split into separate pump and probe paths by a beamsplitter (R = 10%). In the more powerful arm the beam is frequency-doubled to 400 nm using a β-barium borate (BBO) crystal. The energy of the 400 nm pulses is controlled through polarisation rotation with a half-wave plate ($\lambda/2$) before the BBO crystal, as the upconversion efficiency is polarisation-dependent. The 400 nm beam is used as pump beam in the experiment, while the remaining infrared light in this path is blocked using colour filter. The arrival time of the pump pulses at the sample is controlled using a mechanical delay line (Physik Instrumente). We used the less powerful output of the first beamsplitter as the probe beam. The wavelength of this arm is kept at 800 nm. The pump and probe beams are recombined using a dichroic mirror and sent into the focusing objective (Olympus LCPLN20XIR, x20, numerical aperture (NA) 0.45). The beam diameter in the sample plane is approximately 1 μm for both pump and probe. The pump and probe beams are collinear and illuminate the sample at normal incidence. The pump power incident on the sample is 1.2 mW, which corresponds to a fluence of 0.06 J/cm^2. We detect the reflectivity changes as function of time delay by directing the reflected probe beam onto a silicon photodiode. The photodiode signal is sent to a lock-in amplifier (LIA) after being low-pass filtered ($f_{cut-off}$ = 12.5 kHz). The LIA is referenced by the driving signal of the chopper wheel used to modulate the pump excitation. The LIA then acts as a band-pass filter, selectively amplifying the modulated pump-induced signal above the broadband white noise background.

2.2. Spatially resolved layer thickness determination

Figure 2(a) shows the relative reflectivity change $\Delta R/R$ as function of time delay between pump and probe, for gold layers with two different thicknesses. The sharp feature near zero time delay reveals the excitation of the free electrons [20–22]. At longer delay the signal becomes oscillatory, which is a sign of the propagation of the acoustic wave packets inside the metal layer. These signals are a complex superposition of multiple contributions to the local strain, also including effects of local surface heating and surface waves. From a detailed analysis [12], we find that for

Optics EXPRESS

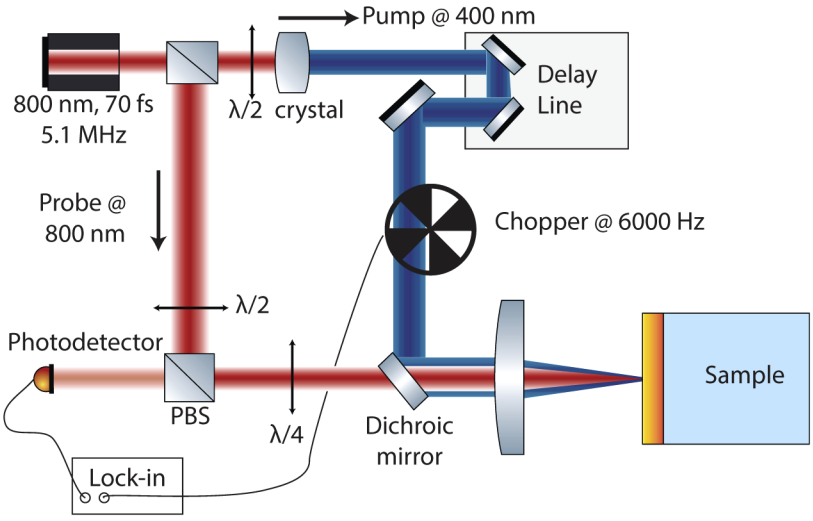

Fig. 1. Schematic of the pump-probe setup used to measure time-dependent reflectivity changes. A 90-10 beam splitter at the output of the laser divides the beam in pump and probe. BBO: Beta-barium borate crystal for frequency doubling. $\lambda/2$: half-wave plate. $\lambda/4$: quarter-wave plate. PBS: polarising beamsplitter. See text for details.

gold surfaces the dips in the reflectivity correspond to the returning acoustic echo. The period that characterizes these oscillations depends on the speed of sound in the material and the layer thickness. Therefore, a Fourier transform of the measured reflectivity curve (Fig. 2(b)) provides a measurement of the local layer thickness.

With acoustic frequencies in the range of 10 GHz as shown in this example, the corresponding acoustic wavelength is actually only around 320 nm, which is below the optical diffraction limit. Therefore, even with tightly focused beams, a thickness determination can be performed at a transverse spatial resolution limited by the optical spot size rather than the acoustic wavelength. This feature enables high-resolution microscopic imaging through metal layers, using the laser-induced acoustic waves as an intermediary, without loss of spatial resolution compared to conventional light-based microscopy. To record a spatial map of layer thickness, we mount the sample on a 3D piezo-driven translation stage (Smaract GmbH). We define the optical axis as 'z', with the transverse plane containing the 'x'- and 'y'-axis. We raster-scan the surface of the sample and perform a pump-probe delay scan at each point.

In the measured signal in Fig. 2(a), an offset at negative time delays is visible (as $\Delta R/R = 0$ is the calibrated reflectivity without pump light). We find that this background level depends on layer thickness and pump power, suggesting that it is due to a cumulative heating effect caused by the relatively high repetition rate of the laser. In particular for thinner layers, the energy deposited by consecutive pulses cannot diffuse out of the excitation region completely, increasing the temperature of the sample and resulting in a refractive index change. This effect does not affect the thickness determination as it does not change the measured oscillation frequency.

2.3. Sample fabrication

To characterize our imaging system and test its capabilities, we fabricated several samples. The sample fabrication consisted of depositing metal layers of controllable thickness onto a glass substrate (SiO_2, 170 μm thick), and subsequently printing patterns on the metal-air interface using two different nano-lithographic procedures: UV lithography and focused ion beam (FIB) milling. The UV lithography has been used for gratings with a pitch of 6 μm and 50% duty cycle

Optics EXPRESS

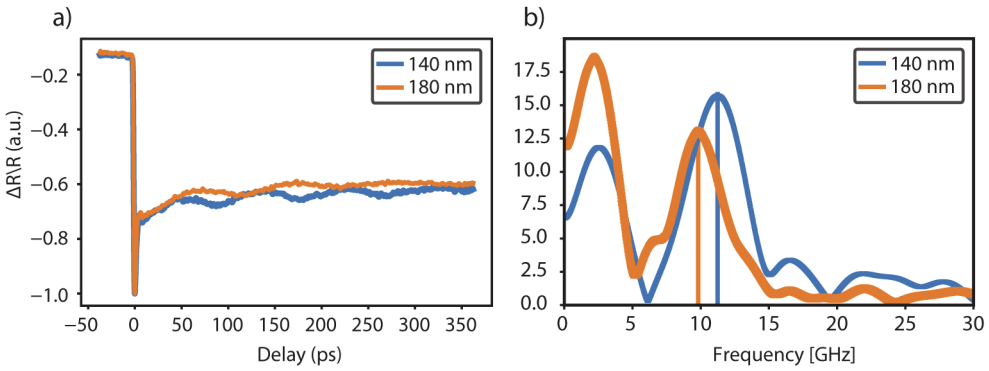

Fig. 2. a) Typical pump-probe delay scan for a single gold layer with two different thicknesses, 140 nm (blue line) and 180 nm (orange). After the sharp response at zero delay, the signals oscillate with a period that depends on the thickness and speed of sound. b) The Fourier transform of the delay scans after removing the contribution of the strong zero-time-delay spike. The vertical lines intersect the x-axis at the frequency that corresponds to a round trip of an echo through the thickness of the layer. The frequency value is used to calculate the period of the oscillation and subsequently the thickness of the layer.

on a thick metal layer. Finally, the FIB has been used to fabricate samples with non-periodic patterns.

In order to make the patterns appear as buried structures, we performed the measurements illuminating the samples from the glass side, generating acoustic waves at the glass-metal interface. This approach was chosen as it ensures a flat interface without any residual topography that might resemble the underlying object structure.

3. Results

3.1. Imaging buried periodic structures

We first performed pump-probe experiments on the grating sample to determine the accuracy with which the thickness is measured as function of position in the transverse direction. Figure 3(a) shows a schematic of the sample fabricated using the UV lithography. The gold (Au) gratings with an amplitude of 10 nm and a pitch of 6 μm are fabricated on top of a 500 nm thick uniform Au layer. On this sample we perform spatially resolved pump-probe measurements as explained in the previous section. The change in reflectivity as function of delay time is shown in Fig. 3(b). The two measurements have been taken from the glass side at two different points in correspondence of the top and the valley of the grating. Similar curves are recorded for a larger area. We move the sample stage with steps of 1 μm in the x direction and 1 μm in y, covering a 4 x 31 μm^2 area. The time traces recorded at each spatial position have an oscillatory part caused by the acoustic waves travelling along the longitudinal direction. The accuracy with which this temporal periodicity is estimated determines the measurement accuracy of the layer thickness. In time domain, the maximum achievable accuracy is limited by the probe pulse duration of 70 fs, but the sampling of the temporal scan and the accuracy of the frequency determination also need to be considered.

The temporal sampling time is linked to the integration time of the LIA, which was set to 3 ms. The delay line scans the pump-probe delay at 40 ps per second, leading to a temporal averaging over 120 fs for every data acquisition. The digital acquisition card (DAQ) records data at 1 kHz. For a speed of sound in Au of 3240 m/s, a time resolution 120 fs corresponds to a height sensitivity of 0.39 nm.

Optics EXPRESS

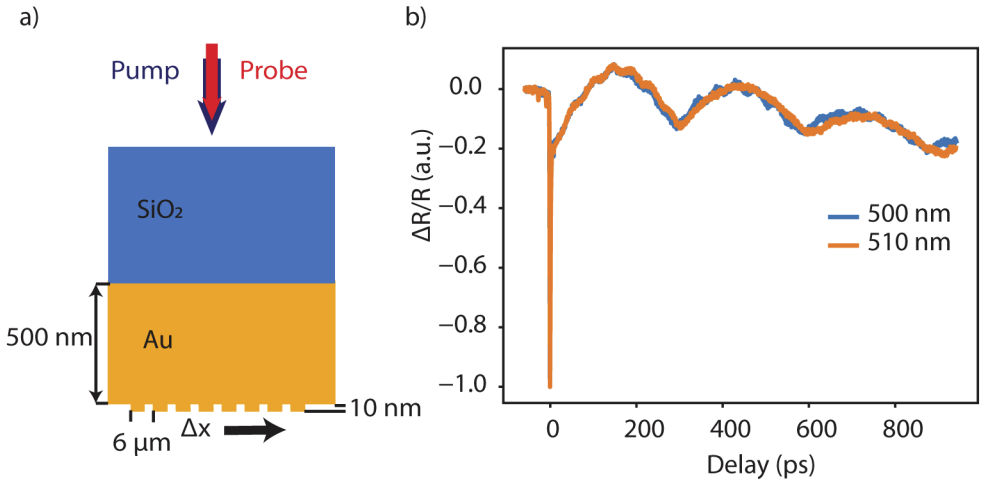

Fig. 3. a) Schematic of the buried grating samples. The pump-probe experiments are done from the glass side of the sample, which consists of a uniform gold layer with a patterned grating on the metal-air interface. b) Photoacoustic measurements at two different positions on the sample corresponding to the top and bottom of the grating. The thickness at these two positions is 500 nm (blue line) and 510 nm (orange), respectively.

A standard approach to obtain the periodicity of an oscillatory signal is to look at its Fourier transform and localize the frequency component that has the highest contribution to the signal. In practice, the achievable accuracy in thickness is therefore mainly limited by the accuracy of the acoustic frequency determination. For the grating in Fig. 3(a) the expected difference in time delay for one round-trip of the acoustic wave at the peaks and valleys of the gratings is 6 ps, on a total delay time of 310 ps, which is the round trip period of an echo in a 500 nm gold layer. While this time delay difference is larger than the temporal resolution of the measurement, the small relative difference in signal strength combined with the relative wide width of the acoustic frequency profiles (Fig. 2(b)) requires an accurate determination of the exact echo timing from the measured data, which can be challenging especially in the case of limited signal-to-noise ratio (SNR). An alternative approach better suited for echo timing determination on our thick Au samples is to fit the time-domain signals directly [12]. To this end, we apply a numerical low pass filter (f_{cut}=30 GHz) and perform a least-squares fit of the filtered data to a damped oscillator model $y_s = A \cdot e^{\alpha_{osc} t} \sin(2\pi f t + \phi)$. However, since the oscillatory signal is on top of a slowly decaying background, we introduce two extra terms in the model: $y_b = A_e \cdot e^{\alpha_e t} + A_b \cdot e^{\alpha_{osc} t} \sin(2\pi f_b t + \pi/2)$. The complete model is the sum of y_s and y_b. The fit is done for all traces measured at different points on the rastered area. The background is determined only for one spatial location and kept constant for all others. In this way we retrieve the oscillation period, from which the local layer thickness can be calculated with a well-defined fit uncertainty. The fit procedure returns the variance that is used to calculate the interval of confidence ($\pm 3\sigma$). The result is shown in panel a of Fig. 4, and shows good agreement with the nominal values. The Au layer thickness was found to be 487 ± 2 nm. To obtain an independent validation of the measured thickness, we perform atomic force microscopy (AFM) measurements on the grating side of the sample, near the edge of a cleared area in the gold layer (Fig. 4(b)). The measured Au layer thickness was 486 ± 2 nm. A direct comparison between the photoacoustic measurement and the AFM measurement is given in Fig. 4(c), showing a line-out in the direction perpendicular to the grating lines for both measurement methods. The photoacoustic data are an average of the 4 data points along the vertical direction of Fig. 4(a). The error bar mainly

Optics EXPRESS

results from the fit uncertainty of the thickness measurements for the individual scan points. There is a good agreement in terms of the determination of the height of the grating lines: some deviations in the transverse shape can be seen, although these are mostly within the photoacoustic measurement uncertainty.

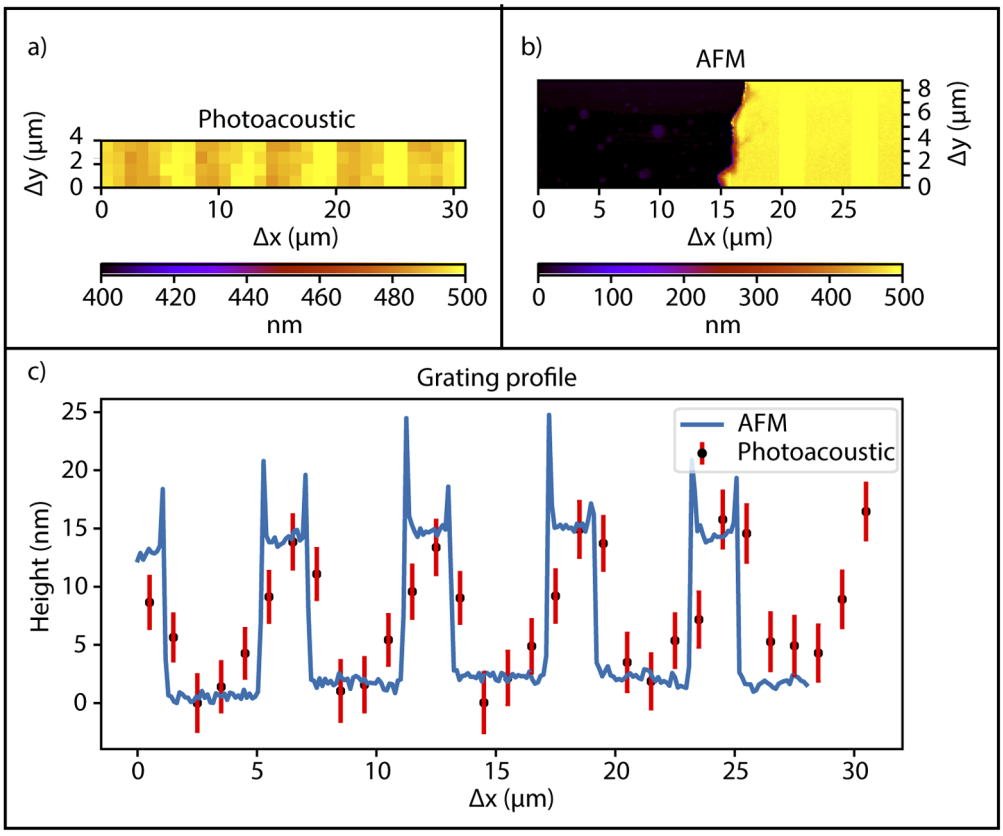

Fig. 4. Photoacoustic imaging of a 10 nm amplitude grating underneath a 500 nm thick layer of gold. a) The measured height map obtained by making a delay scan per pixel. Thickness reconstruction using time-domain fitting. See text for details on the model used for the fit. b) AFM measurement near an edge of the coated layer, showing the total grating thickness. c) Comparison of AFM and photoacoustic measurements, averaged along the y-direction for a range as shown in Fig. 4(a). The photoacoustic measurement points are offset by the absolute measured height of 487 nm.

3.2. *Non-periodic structures and image resolution*

To prove the versatility of our imaging system, we have extended the measurements to imaging of non-periodic structures.

Reference images of the studied samples are displayed in Figs. 5(a) and (b). These samples contain the logo of our institute (ARCNL) and a map of Amsterdam, which have been patterned into a 270 nm and 200 nm Au layer respectively using a Focused Ion Beam (FIB). Two separate versions of the institute logo were produced, differing only in the step height between the logo and its surroundings (being 60 and 120 nm). An AFM image of the 60-nm-depth sample is shown in Fig. 5(c).

Optics EXPRESS

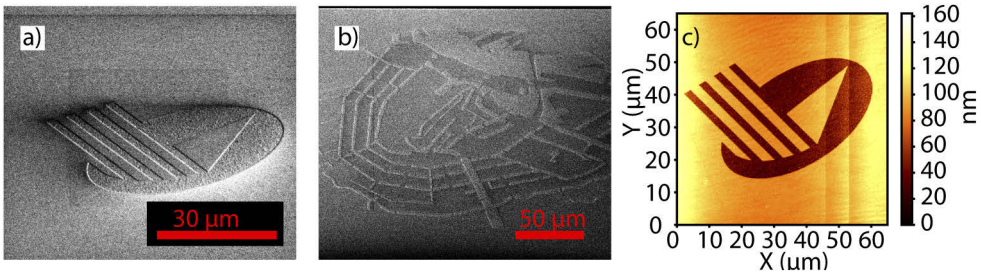

Fig. 5. a) Scanning electron microscope (SEM) image of the ARCNL logo, fabricated using Focused Ion Beam (FIB) milling. The patterns were milled 60 nm deep into a 270 nm thick Au layer. b) SEM image of a map of Amsterdam also produced by FIB, milled 50 nm deep into a 200 nm thick Au layer. c) AFM image of the ARCNL logo, showing the 60 nm thickness difference.

Spatially resolved photoacoustic measurements are performed on both logo samples, and the results are shown in Figs. 6(a) and (b). The image size is 60 µm by 30 µm, obtained with a step size of 2 µm in both directions. The thickness determination is performed using the time-domain fitting procedure discussed in the previous section, and shows quantitative agreement with the nominal values. Each spatial pixel required a time-domain scan of ≈20 seconds, resulting in a measurement time of 3 hours for the full image.

To improve the image acquisition speed, the pump-probe delay can be set to a fixed value determined from a single time-delay scan at a reference position. A spatial raster scan at such a constant time delay can then still provide image contrast for buried layers, although at the cost of losing the absolute layer thickness information [18]. Examples of such measurements on the 60-nm-deep logo sample are shown in Figs. 6(c)-(e), where we set the pump-probe time delay to different values around the arrival time of the first acoustic echo from the flat Au layer, and measure the sample reflectivity as a function of position by spatially scanning the sample along the focused beams. Each horizontal scan is performed by continuous motion at constant velocity, after which a discrete vertical step of 1 µm is taken. With this approach, recording each image in Figs. 6(c)-(e) takes 2 minutes. We emphasize that this measurement method only provides reflection-based image contrast rather than quantitative layer thickness information: by setting the time delay to different values, the contrast changes strongly and can even be inverted. The change in contrast between the logo and the surrounding are visible in Figs. 6(c)-(e) for different delay time. In Fig. 6(f), the time traces for a scan position at the logo and at the surrounding area are shown. A large difference in $\Delta R/R$ results in higher image contrast. In Fig. 6(c), 120 ps time delay corresponds to the expected peak of the first echo from the logo. At a 180 ps time delay (Fig. 6(d)), which is close to the expected arrival time of the echo from the structure surrounding the logo, the contrast between logo and surroundings diminishes. The contrast increases again towards the second echo from the logo at 240 ps (Fig. 6(e)). In a scanning-probe imaging method as employed here, the achievable transverse resolution is ultimately limited by the focal spot size. In addition, the step size of the spatial scan needs to be chosen smaller than the laser spot size to avoid undersampling issues. Using a continuous scan of the stage this requirement is satisfied at an acquisition rate of 1 kHz and a stage speed of 20 µm/s. To characterize the transverse resolution of our imaging system we use an edge response method [23]. The reflectivity changes near the edge of the tilted lines in the logo shown in Fig. 6(c) are used to reconstruct an oversampled edge function. Multiple horizontal scans of the leftmost line at increasing ΔY positions are recorded, subsequently aligned, and used to least-squares fit an edge response function (Fig. 7(a)). The derivative of the determined edge response function gives the line response, and a Fourier transform of this line response function yields the modulation

Optics EXPRESS

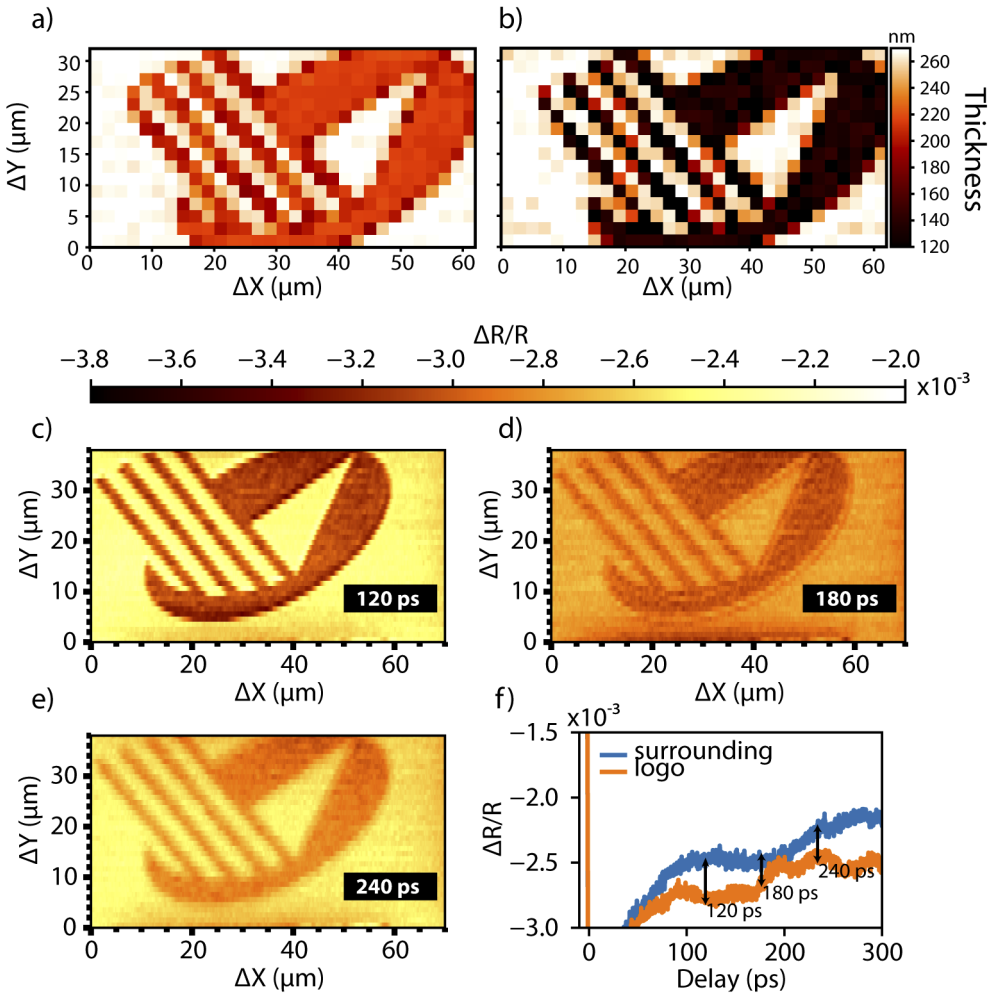

Fig. 6. Photoacoustic measurements on the ARCNL logo below a 270 nm thick gold layer. (a),(b) Spatially resolved thickness measurements on samples with depths of 60 nm (a) and 120 nm (b). (c-e) Photoacoustic measurements on the 60-nm-depth structure with a fixed delay between pump and probe. The three images are taken at different time delay settings. These measurements are significantly faster, but do not provide quantitative thickness information. (f) Part of the time-delay scan for the spatial positions at and next to the logo sample, for the range including the time delays of images (c-e).

transfer function (MTF) that is typically used to define the resolution of optical systems [24]. The resulting normalized MTF for our system is shown in Fig. 7(b): the 10% value is typically taken as the number of line pairs that the imaging system can resolve. We find a value of 0.83 line pairs per μm, meaning a spatial resolution of 1.2 μm. This resolution is close to the Rayleigh diffraction limit at 0.45 NA, given by 0.61 λ/NA = 1.1 μm, and is consistent with the measured spot sizes of pump and probe.

The improved acquisition speed of the fixed-time-delay method allows imaging of millimeter scale structures with no compromise in imaging resolution. To demonstrate this important aspect we fabricated such a sample, shown in Fig. 5(b). The sample is a map of the canals of Amsterdam, with spatial dimensions of 250 × 250 μm^2. We use the FIB to draw the map on a 200 nm gold

Optics EXPRESS

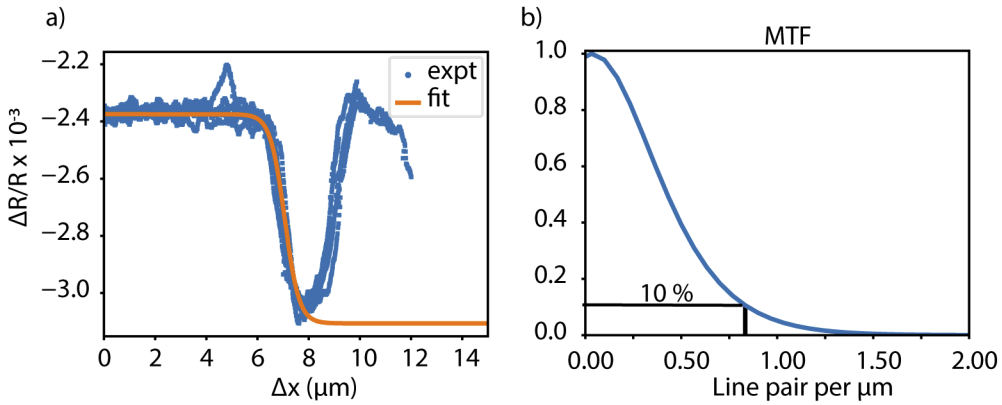

Fig. 7. a) Reflectivity change as a function of scan position for a 1D scan across a diagonal line on the left side of the ARCNL logo (Fig. 6(c)), at various ΔY positions (scans corrected for horizontal displacement as function of ΔY). Least-squares fitting yields the edge response function. b) The modulation transfer function (MTF), which is the Fourier transform of the derivative of the edge response function. The 10% value corresponds to the maximum number of line pairs per μm that can be resolved.

layer and remove 50 nm from the exposed area. A photoacoustic measurement at a fixed time delay of 110 ps is shown in Fig. 8. A good contrast image of the map is obtained scanning a length of 350 μm at 40 μm/s along the x-direction and a length of 400 μm in steps of 2 μm along the y-direction. The map contains various 1 – μm-size features, which are well resolved without significant loss of contrast even comparing with the SEM image (Fig. 5(b)).

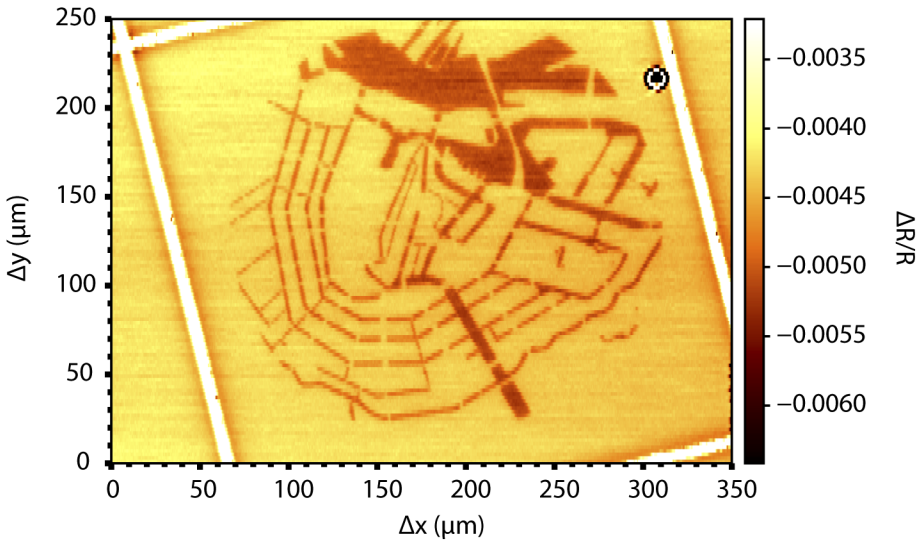

Fig. 8. Photoacoustic measurement of the Amsterdam canal map sample buried underneath a 150 nm thick gold layer. The pump-probe time delay was fixed at 110 ps.

Optics EXPRESS

4. Conclusion

We have developed a scanning-probe photoacoustic microscope that enables high-resolution imaging of microscopic structures buried below optically opaque layers. A fitting procedure has been used to determine the thickness of the layer, reconstructing height maps of buried objects with an accuracy of 2 nm. We note that the achievable depth sensitivity is dependent on material properties, which determine the frequency content of the acoustic wave. As gold supports only limited acoustic frequencies, even higher depth sensitivity may be expected for other metals. We have recorded images of spatially non-periodic structures with sub-μm feature sizes, using pump-probe scans at discrete spatial positions, as well as continuous scans at fixed pump-probe time delay. From these images we have characterized the spatial resolution of the imaging system by determining its MTF, which resulted in a near-diffraction-limited spatial resolution of 1.2 μm.

We compared the photoacoustic measurement to an AFM measurement, which showed good agreement in the height determination of the grating structure. Furthermore, we emphasize that our measurement method is non-invasive as it operates well below the damage threshold of the opaque layer. Future improvements to the SNR such as higher-frequency LIA methods can be envisaged, further improving sensitivity and imaging speed. We therefore see applications of this imaging approach in materials science and the characterization of semiconductor nanostructures, among others.

Funding

Nederlandse Organisatie voor Wetenschappelijk Onderzoek; European Research Council (ERC Starting Grant 637476).

Acknowledgments

We thank Irwan Setija, Simon Huisman and Bas Goorden for insightful discussions. This work was conducted at the Advanced Research Center for Nanolithography, a public-private partnership between the University of Amsterdam, Vrije Universiteit Amsterdam, the Netherlands Organization for Scientific Research (NWO), and the semiconductor-equipment manufacturer ASML.

Disclosures

The authors declare no conflict of interest.

References

1. A. J. den Boef, "Optical wafer metrology sensors for process-robust CD and overlay control in semiconductor device manufacturing," Surf. Topogr.: Metrol. Prop. **4**(2), 023001 (2016).
2. H. Schwenke, U. Neuschaefer-Rube, T. Pfeifer, and H. Kunzmann, "Optical methods for dimensional metrology in production engineering," CIRP Ann. **51**(2), 685–699 (2002).
3. N. Mokhlesi and R. Scheuerlein, "Three dimensional nand memory," US Patent US7851851B2 (2007).
4. H. Kim, S. Ahn, Y. G. Shin, K. Lee, and E. Jung, "Evolution of nand flash memory: From 2d to 3d as a storage market leader," in *2017 IEEE International Memory Workshop (IMW)*, (2017), pp. 1–4.
5. S. Edward, H. Zhang, I. Setija, V. Verrina, A. Antoncecchi, S. Witte, and P. Planken, "Detection of hidden gratings through multilayer nanostructures using light and sound," Phys. Rev. Appl. **14**(1), 014015 (2020).
6. C. Thomsen, H. T. Grahn, H. J. Maris, and J. Tauc, "Surface generation and detection of phonons by picosecond light pulses," Phys. Rev. B **34**(6), 4129–4138 (1986).
7. C. Thomsen, H. Maris, and J. Tauc, "Picosecond acoustics as a non-destructive tool for the characterization of very thin films," Thin Solid Films **154**(1-2), 217–223 (1987).
8. A. G. Every and W. Sachse, "Determination of the elastic constants of anisotropic solids from acoustic-wave group-velocity measurements," Phys. Rev. B **42**(13), 8196–8205 (1990).
9. O. B. Wright, "Ultrafast nonequilibrium stress generation in gold and silver," Phys. Rev. B **49**(14), 9985–9988 (1994).
10. J. A. Rogers, A. A. Maznev, M. J. Banet, and K. A. Nelson, "Optical generation and characterization of acoustic waves in thin films: Fundamentals and applications," Annu. Rev. Mater. Sci. **30**(1), 117–157 (2000).

Optics EXPRESS

11. B. Audoin, M. Perton, N. Chigarev, and C. Rossignol, "Diffraction of picosecond bulk longitudinal and shear waves in micron thick films; application to their nondestructive evaluation," Ultrasonics **48**(6-7), 574–577 (2008). Selected Papers from ICU 2007.
12. H. Zhang, A. Antoncecchi, S. Edward, I. Setija, P. Planken, and S. Witte, "Unraveling phononic, optoacoustic, and mechanical properties of metals with light-driven hypersound," Phys. Rev. Appl. **13**(1), 014010 (2020).
13. P. Ruello and V. E. Gusev, "Physical mechanisms of coherent acoustic phonons generation by ultrafast laser action," Ultrasonics **56**, 21–35 (2015).
14. O. Matsuda, M. C. Larciprete, R. L. Voti, and O. B. Wright, "Fundamentals of picosecond laser ultrasonics," Ultrasonics **56**, 3–20 (2015).
15. O. B. Wright and K. Kawashima, "Coherent phonon detection from ultrafast surface vibrations," Phys. Rev. Lett. **69**(11), 1668–1671 (1992).
16. O. B. Wright and V. E. Gusev, "Acoustic generation in crystalline silicon with femtosecond optical pulses," Appl. Phys. Lett. **66**(10), 1190–1192 (1995).
17. B. C. Daly, N. C. R. Holme, T. Buma, C. Branciard, T. B. Norris, D. M. Tennant, J. A. Taylor, J. E. Bower, and S. Pau, "Imaging nanostructures with coherent phonon pulses," Appl. Phys. Lett. **84**(25), 5180–5182 (2004).
18. S. Ramanathan and D. G. Cahill, "High-resolution picosecond acoustic microscopy for non-invasive characterization of buried interfaces," J. Mater. Res. **21**(5), 1204–1208 (2006).
19. T. Saito, O. Matsuda, M. Tomoda, and O. B. Wright, "Imaging gigahertz surface acoustic waves through the photoelastic effect," J. Opt. Soc. Am. B **27**(12), 2632–2638 (2010).
20. J. Hohlfeld, S.-S. Wellershoff, J. Güdde, U. Conrad, V. Jähnke, and E. Matthias, "Electron and lattice dynamics following optical excitation of metals," Chem. Phys. **251**(1-3), 237–258 (2000).
21. S.-S. Wellershoff, J. Güdde, J. Hohlfeld, J. Muller, and E. Matthias, "Role of electron-phonon coupling in femtosecond laser damage of metals," Proc. SPIE **3343**, 378–387 (1998).
22. S. Edward, A. Antoncecchi, H. Zhang, H. Sielcken, S. Witte, and P. C. M. Planken, "Detection of periodic structures through opaque metal layers by optical measurements of ultrafast electron dynamics," Opt. Express **26**(18), 23380–23396 (2018).
23. S. Najafi and K. Madanipour, "Measurement of the modulation transfer function of a charge-coupled device array by the combination of the self-imaging effect and slanted edge method," Appl. Opt. **52**(19), 4724–4727 (2013).
24. J. W. Coltman, "The specification of imaging properties by response to a sine wave input," J. Opt. Soc. Am. **44**(6), 468–471 (1954).

192.87.153.201 {ts '2020-10-28 07:11:36'}